RESEARCH ARTICLE

Reduced-order modeling of high-speed jets controlled by arc filament plasma actuators

Aniruddha Sinha · Andrea Serrani ·
Mo Samimy

Abstract Arc filament plasma actuators applied to high-speed and high Reynolds number jets have demonstrated significant mixing enhancement when operated near the jet column mode (JCM) frequency. A feedback-oriented reduced-order model is developed for this flow from experimental data. The existent toolkit of stochastic estimation, proper orthogonal decomposition, and Galerkin projection is adapted to yield a 35-dimensional model for the unforced jet. Explicit inclusion of a "shift mode" stabilizes the model. The short-term predictive capability of instantaneous flow fields is found to degrade beyond a single flow time step, but this horizon may be adequate for feedback control. Statistical results from long-term simulations agree well with experimental observations. The model of the unforced jet is augmented to incorporate the effects of plasma actuation. Periodic forcing is modeled as a deterministic pressure wave specified on the inflow boundary of the modeling domain. Simulations of the forced model capture the nonlinear response that leads to optimal mixing enhancement in a small range of frequencies near the JCM.

Abbreviations
JCM   Jet column mode
LAFPA   Localized arc filament plasma actuator

A. Sinha · A. Serrani · M. Samimy (✉)
The Ohio State University, Columbus, OH 43210, USA
e-mail: samimy.1@osu.edu

Present Address:
A. Sinha
California Institute of Technology, Pasadena, CA 91106, USA

POD   Proper orthogonal decomposition
ROM   Reduced-order model
SLSE   Spectral linear stochastic estimation

1 Introduction

High-speed turbulent flows represent nonlinear, infinite-dimensional systems that pose one of the frontiers of feedback control today. The development of reduced-order models (ROM) for approximating the dynamics of such flows is still in its infancy. Although useful linear models have been proposed for some flow control problems (e.g., Rowley 2005), nonlinear effects cannot be neglected for most flows. The majority of research in the latter category has focused on flows dominated by oscillations at a few discrete frequencies—for example—vortex shedding from bluff bodies and airfoils, cavity tones (e.g. Caraballo et al. 2008; Noack et al. 2010). Modeling is rendered considerably more difficult if the flow is characterized by large-scale structures with broadband frequency content. The most relevant flows in this class are turbulent planar shear layers, jets, and high-speed boundary layers. Pioneering work in reduced-order modeling of flows was in fact aimed at isolating and analyzing the essential dynamics of the turbulent near-wall flow in an open channel (Aubry et al. 1988). Notable advances have also been made in the modeling of unforced axisymmetric jets (e.g., Zheng and Glauser 1990; Schlegel et al. 2012; Kerherve et al. 2012) and planar shear layers (e.g., Ukeiley et al. 2001).

One of the consequences of turbulent interactions in the jet shear layer is noise. Although jet noise is a mature research area with a history spanning six decades, there is still a lack of consensus on the fundamental mechanisms

involved. However, it is commonly recognized that the large-scale coherent structures in the jet mixing layer play an important role, especially near the end of the potential core. Apart from jet noise mitigation, research effort is also focused on enhancing mixing in jets. The rate of dissipation is correlated with the dynamics of the large-scale structures in the jet shear layer. Affecting the turbulence characteristics of flows by manipulating large-scale structures is within the realm of flow control, which is therefore appropriate for both these applications.

Localized arc filament plasma actuators (LAFPA) have been developed and continuously improved for flow control applications in the gas dynamics and turbulence laboratory (GDTL) at the Ohio State University. LAFPAs are capable of generating high-amplitude and high-bandwidth control signals, which are crucial actuator characteristics for manipulating high-speed and high Reynolds number flows. These actuators provide intense but controlled localized Joule heating to manipulate the large-scale structures in the mixing layer by exciting the natural instabilities of the jet. Operation of the LAFPAs near the jet column mode (JCM) frequency (Crow and Champagne 1971) results in maximum mixing enhancement with significant reduction in the potential core length, and increase in turbulence (Samimy et al. 2007a; Kearney-Fischer et al. 2009; Samimy et al. 2010). Plasma actuation at higher frequencies attenuates far-field noise up to ∼2 dB over a range of practical operating conditions (e.g., Samimy et al. 2007b).

Optimal actuator parameters for a certain application exist in a limited region of the parameter space. Moreover, as in any control system, the optimal parameters in open-loop are functions of the jet operating conditions (e.g., Mach number and exit temperature) which are subject to variations and uncertainties in flight. Thus, a natural advancement toward practical implementation is to incorporate feedback control, which may guarantee robustness in the presence of such uncertainties.

Development of feedback controllers for high-speed jets forced with LAFPAs is an ongoing effort at GDTL. A preliminary attempt was a model-free extremum-seeking technique developed and implemented in experiments (Sinha et al. 2010a). Although the simplicity of model-free controllers is attractive for flow control, their responsiveness is generally slowed by the necessity of neglecting the system dynamics. The first step in model-based feedback control for improved responsiveness is the design of a sufficiently accurate model of the *unforced* jet. Such a ROM was built using stochastic estimation, proper orthogonal decomposition (POD), and Galerkin projection for use with data that can be feasibly measured in experiments (Sinha et al. 2010b). An indispensable tool for the development and validation of the modeling strategy was

the direct numerical simulation (DNS) data of a low Reynolds number Mach 0.9 jet created by Freund (2001). The outcome was a technique that is hereby applied to the much reduced information contained in the experimental data. Although the general validity of the POD–Galerkin approach for modeling turbulent fluid dynamics is a matter of debate (see e.g. Rempfer 2000), its suitability for the present problem was established by Sinha et al. (2010b) and further reinforced here.

The design of feedback laws requires the ROM to explicitly incorporate the effect of actuation. A mathematically rigorous option for linear models is balanced POD (Rowley 2005). For nonlinear flows, availability of time-resolved empirical data allows the application of standard system identification techniques. High-speed flows of present interest do not satisfy either of the above requirements, and phenomenological approaches are necessary.

Flow control actuators can be broadly divided into two categories based on the nature of their coupling with the flow; strategies for modeling them differ likewise. Actuators can produce a body force, for example, AC dielectric barrier discharge (AC–DBD) plasma actuators. Since the body force appears as an additive term in the Navier–Stokes equation, the incorporation of its amplitude in the reduced-order model is particularly straightforward (e.g., Rowley 2005). On the other hand, the majority of actuators studied inject momentum into the flow at a physical boundary, for example, zero net mass flux devices, steady or pulsed blowing and/or suction, and boundary movement. Since boundary effects are local in time and space whereas low-dimensional spatial bases are global in space, indirect methods are required for modeling such actuators (e.g., Caraballo et al. 2008). LAFPAs may be categorized as boundary actuators that excite instabilities in the flow. Due to experimental constraints that would become clear below, the domain of the empirical model of the jet cannot include the site of introduction of the plasma perturbations. As a workaround, a phenomenological model of actuation is proposed in this work.

Large–eddy simulation (LES) has been able to replicate most of the qualitative features of LAFPA forcing as well as many of the relevant statistical trends (Gaitonde and Samimy 2011). The actuators are modeled as local temperature pulses at the lip of the nozzle. The operating conditions mimicked the Mach 1.3 jet at GDTL. The computations have provided a wealth of physical insight into the mechanism of the actuation. In addition to experimental data, this LES database informs the development of the ROM described herein.

Forcing the jet near the JCM frequency for mixing enhancement organizes the large-scale structures, which facilitates the low-dimensional description of the dynamics. Forcing at the higher frequencies required for noise

attenuation has the opposite effect on the coherent structures, and many more modes would be needed for successful modeling. The present article focuses on the first problem as a feasible test bench for the modeling paradigm.

The formulation of the ROM for unforced jets is briefly revisited in Sect. 2. This motivates the design of the experiments discussed in Sect. 3. Results of applying the modeling technique to the experimental data are presented in Sect. 4. The phenomenological model of LAFPA actuation is described and validated in Sect. 5. Conclusions are discussed in Sect. 6.

2 ROM of unforced jet

A brief description of the technique for modeling unforced jets using empirical data is provided below; the details can be found in Sinha et al. (2010b). It is noted at the outset that an assumption of incompressibility has been shown to be appropriate (Sinha 2011). In particular, a compressible POD–Galerkin model [following Gloerfelt (2008)] derived from the DNS database was found to be no more accurate than the incompressible model. In any case, it is infeasible to acquire the data required for deriving a compressible ROM in the present experiments.

A cylindrical modeling domain of the unbounded axisymmetric jet encompassing the shear layer in the vicinity of the end of the potential core is chosen since it is most pertinent for the control objectives at hand (see Fig. 1). All velocities and linear coordinates are normalized by the nozzle exit velocity U_j and diameter D, respectively. Time and pressure are normalized respectively by the flow timescale D/U_j and the jet dynamic head $\rho_j U_j^2$, where ρ_j is the nozzle exit density. With kinematic viscosity at the exit denoted by v_j, the pertinent Reynolds number is $Re := U_j D/v_j$. Frequencies f are normalized by the reciprocal of the flow timescale to obtain the Strouhal number $St_D = fD/U_j$.

In cylindrical coordinates (x, r, θ), the modeling domain is $\Omega := [X_1, X_2] \times [0, R] \times \mathbb{T}$. Here, X_1 and X_2 are the upstream and downstream bounds of the axial domain, R is the radial extent of the domain, and $\mathbb{T}$ is the circle group. The velocity is $\mathbf{U}: \Omega \times \mathbb{R} \to \mathbb{R}^3, \mathbf{U}: (x, r, \theta, t) \mapsto (U_x, U_r, U_\theta)^\mathrm{T}$. With stationarity and axisymmetry assumed, the mean velocity is $\overline{\mathbf{U}}(x, r) := E\big[1/(2\pi) \int_{-\pi}^{\pi} \mathbf{U}(x, r, \theta, t) \mathrm{d}\theta\big]_t$, where the expectation operator $E[\cdot]_t$ signifies average over time t. The fluctuating velocity is $\mathbf{u}(x, r, \theta, t) := \mathbf{U}(x, r, \theta, t) - \overline{\mathbf{U}}(x, r)$. The corresponding Reynolds decomposition for pressure P is written as $p := P - \overline{P}$.

The POD along the homogenous and periodic azimuthal direction is equivalent to an azimuthal Fourier transform, and it is performed first:

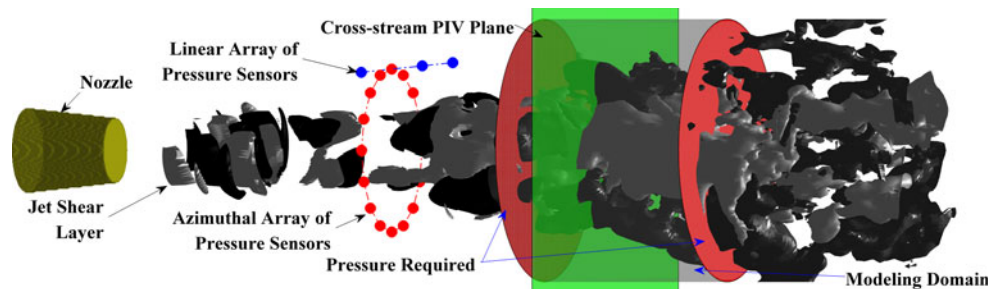$$\mathbf{u}(x, r, \theta, t) = \sum_{m=-M}^{M} \hat{\mathbf{u}}(x, r, t; m) \mathrm{e}^{\mathrm{i}m\theta},$$

$$\hat{\mathbf{u}}(x, r, t; m) := \frac{1}{2\pi} \int_{-\pi}^{\pi} \mathbf{u}(x, r, \theta, t) \mathrm{e}^{-\mathrm{i}m\theta} \mathrm{d}\theta. \quad (1)$$

Here, m is the azimuthal mode, and M is the highest mode retained. The domain of Fourier quantities is $\hat{\Omega} := [X_1, X_2] \times [0, R]$. The pressure field may also be decomposed similarly.

The velocity vector field $\hat{\mathbf{u}}$ belongs to the function space $\mathcal{L}^2_{\hat{\Omega}, m}$ (defined in the Appendix—Sect. 7.1). The associated inner product (also defined in the Appendix) is such that the square of the induced norm $||\cdot||_{\hat{\Omega}, m}$ is the azimuthal modal turbulent kinetic energy (TKE) integrated over the domain. The goal of POD is, given an ensemble of data for $\hat{\mathbf{u}} \in \mathcal{L}^2_{\hat{\Omega}, m}$, to find a subspace $S_m \subset \mathcal{L}^2_{\hat{\Omega}, m}$ of fixed dimension N_m, such that the error $E\big[\|\hat{\mathbf{u}} - \mathcal{P}_{S_m}\hat{\mathbf{u}}\|^2_{\hat{\Omega}, m}\big]_t$ is minimized (Rowley 2002). Here, $\mathcal{P}_{S_m}$ is the orthogonal projection onto the subspace S_m. The classical POD requires the empirical data in the form of two-point correlations over the entire domain. This is onerous to obtain experimentally in the present configuration. The alternative snapshot POD is used instead. To emphasize the availability of velocity field snapshots at discrete time instants t_j, the notation may be modified as $\hat{\mathbf{u}}^j(x, r; m) := \hat{\mathbf{u}}(x, r, t_j; m)$. Then, the POD problem setup is

Fig. 1 Schematic of the axisymmetric jet indicating the modeling domain with the inflow and outflow planes where pressure is to be specified

$$\hat{\mathbf{\Phi}}^n(x, r; m) := \sum_j \beta_j^n(m)\hat{\mathbf{u}}^j, (x, r; m),$$

$$\sum_j \langle \hat{\mathbf{u}}^j, \hat{\mathbf{u}}^k \rangle_{\hat{\Omega},m} \beta_j^n(m) = \Lambda^n(m)\beta_k^n(m). \tag{2}$$

Here, Λ^n and $\hat{\mathbf{\Phi}}^n$ are respectively the eigenvalue and eigenfunction for the nth POD mode, and β_k^n is the coefficient of the kth snapshot toward $\hat{\mathbf{\Phi}}^n$. For later reference, the components of $\hat{\mathbf{\Phi}}^n$ in cylindrical coordinates are $(\hat{\Phi}_x^n, \hat{\Phi}_r^n, \hat{\Phi}_\theta^n)$.

The POD mode number n indexes the eigenvalues in descending order. Then, the first N_m eigenfunctions form the desired optimal basis for the subspace S_m. This allows the following approximate change of coordinates for each azimuthal mode m:

$$\hat{\mathbf{u}}(x, r, t; m) \approx \sum_{n=1}^{Nm} \hat{\alpha}^n(t; m)\hat{\mathbf{\Phi}}^n(x, r; m),$$

$$\hat{\alpha}^n(t; m) = \langle \hat{\mathbf{u}}(\cdot, \cdot, t; \cdot), \hat{\mathbf{\Phi}}^n \rangle_{\hat{\Omega},m} \Big/ \|\hat{\mathbf{\Phi}}^n\|_{\hat{\Omega},m}^2. \tag{3}$$

The direct sum of the subspaces $\left\{ S_m \subset \mathcal{L}_{\hat{\Omega},m}^2 \right\}_{m=0}^M$ creates the subspace $S \subset \mathcal{L}_{\Omega}^2$ wherein the low-dimensional kinematics is defined. Note that symmetry considerations imply that the negative azimuthal modes are not independent from the positive ones, so that the dimension of S is $N_M := \sum_{m=0}^M N_m$. The incompressible Navier–Stokes equations governing the flow can be formally written as $\dot{\mathbf{U}} = \mathcal{N}(\mathbf{U})$, where $\mathcal{N}$ is an operator on $\mathcal{L}_{\Omega}^2$. The goal of reduced-order dynamics modeling is to determine a dynamical system that evolves on S and approximates the original dynamics in some sense (Rowley 2002). Galerkin projection specifies the new vector field on S as the orthogonal projection of $\mathcal{N}$ onto S, yielding

$$\dot{\hat{\alpha}}^n(t; m) = \sum_{n'} \mathcal{G}_L(n, n', m)\hat{\alpha}^{n'}(t; m)$$
$$+ \sum_{m', n'', n'} \mathcal{G}_Q(n, n', n'', m, m')\hat{\alpha}^{n'}(t; m')\hat{\alpha}^{n''}(t; m - m')$$
$$+ \delta_{m,0}\mathcal{G}_C(n) - 2\pi \left| \int_0^R \hat{p}(x, r, t; m)\{\hat{\Phi}_x^n(x, r; m)\}^H r \, dr \right|_{x=X_1}^{X_2}. \tag{4}$$

Here, δ is the Kronecker delta, and $(\cdot)^H$ denotes the Hermitian transpose. The terms in the equation are explained in the Appendix—Sect. 7.2. The pressure term is negligible for unforced jets (Sinha et al. 2010b), but will be important for incorporating actuation effects in forced jets. The dimensionality of S confers the nomenclature "N_M-D ROM" on the above model.

The empirical flow information required is a statistically significant sample of instantaneous snapshots of the flow variables over the *entire* domain. An approximation of such snapshots may be obtained using stochastic estimation (Tinney et al. 2008b). This involves two main steps: (1) determining the correlation between pressure at a fixed location in the irrotational near field and the velocity on a fine-enough grid of points in the desired domain, and (2) using the above correlations and the pressure record to estimate a snapshot of the velocity over the entire domain. The experimental complexity is reduced substantially by performing plane-wise measurements of the velocity field on discrete cross-stream sections as shown in Fig. 1 (Tinney et al. 2008a). The accuracy of approximation is enhanced by employing the spectral variant of linear stochastic estimation (SLSE) owing to the disparity in the spectra of the pressure and velocity fields as well as the convective time lag between the two fields (Tinney et al. 2006, 2008b). The use of the linear array in addition to the azimuthal array of pressure sensors further improves the estimation (Sinha et al. 2010b).

3 Experimental setup

All experiments have been conducted at GDTL. The jet is created using compressed air discharging horizontally through a thick-lipped axisymmetric converging nozzle into an anechoic chamber before exhausting outdoors (see Fig. 2a). The nozzle exit diameter is $D = 25.4$ mm, the Mach number is 0.9, and the jet is not heated. The Reynolds number is $Re \sim 6.7 \times 10^5$.

Each LAFPA consists of a pair of 1 mm diameter tungsten electrodes connected to a high-voltage ($\sim$kV) source through a high-frequency switching circuitry. A boron nitride nozzle extension, with 25.4 mm inner diameter and 15 mm thickness, is used to hold 8 LAFPAs distributed uniformly around the azimuth 1 mm upstream of the exit. The center-to-center distance between the two electrodes in a LAFPA is 3 mm. When the switch to a LAFPA is closed, the voltage across the electrodes ramps up to the breakdown voltage ($\sim$10 kV) in less than 10 μs. The air between the electrodes is ionized, and an electric arc is established. Immediately afterward, the voltage across the electrodes drops to a few hundred volts and remains at that level until the switch is opened. The computer-generated signal that manipulates the switching circuitry is a rectangular pulse train with independent control of frequency, phase, and pulse width. The bandwidth of the actuators is 200 kHz, and the forcing frequency f_F is normalized to define the forcing Strouhal number $St_{DF} = f_F D/ U_j$. The relative phases of the eight actuators is controlled, and forcing can be achieved at azimuthal modes $m_F = 0$–3 as well as modes ±1, ±2, and ±4. The optimal pulse width is $\sim$7 μs (Hahn et al. 2011), and this is used in the

Fig. 2 Schematic of **a** jet experimental facility, and **b** near-field pressure sensing setup
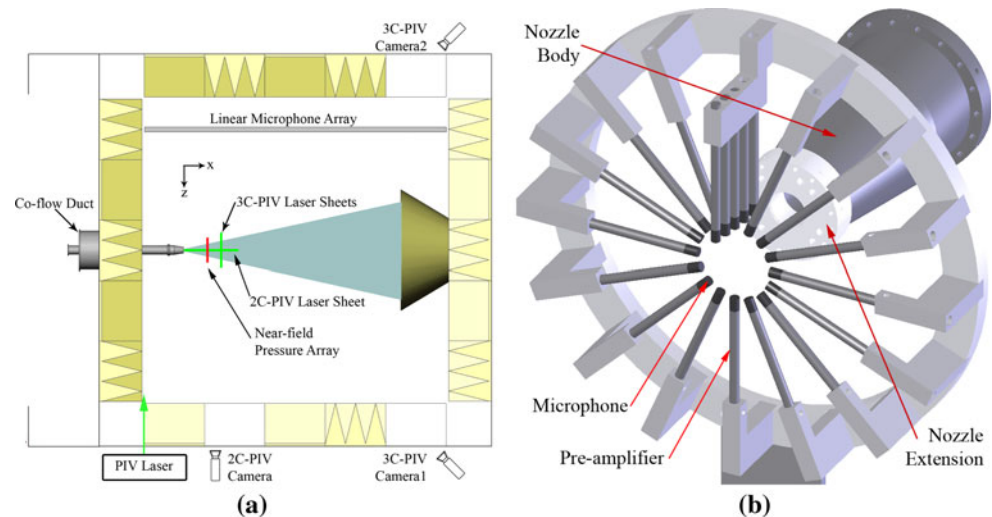
experiments. Note that the amplitude of excitation cannot be controlled independently. More details of LAFPAs can be found in previous publications from GDTL (Utkin et al. 2007; Samimy et al. 2007a, b, 2010).

A LaVision 3-component PIV system is used for velocity measurements on the cross-stream plane of the unforced jet at discrete streamwise locations between $x = 5.0$ and 7.75 ($\Delta x = 0.25$). The PIV is also performed at $x = \{5, 6, 7\}$ for 3 forcing cases near the JCM—viz. $St_{DF} = 0.25, 0.3$, and 0.35; $m_F = 0$. A Spectra Physics model SP-400 dual head Nd:YAG laser is used as the light source. The two 4 MP cameras are placed downstream of the jet exit outside windows in the anechoic chamber and obey the Scheimpflug principle (see Fig. 2a). The jet plume is seeded with diethylhexyl sebacate droplets atomized by a four-jet LaVision atomizer. A 381 mm diameter duct is placed co-axial with the jet to generate a very low-speed ($\sim 0.01 \, U_j$) entrained co-flow seeded by a fogger. The average droplet size is 0.7 and 0.25 μm for the jet flow and co-flow, respectively. Image pairs are separated in time by 1.4 μs, and 1,000 vector maps are recorded at 2 Hz on each plane.

The resolution of the PIV images is ~ 0.1 mm. Post-processing using a three-pass correlation in the DaVis software results in a resolution of $\sim 0.06D$ for the velocity maps. Triangle-based linear interpolation is used to transform the velocity maps to a polar grid. The radial grid has $\Delta r = 0.0625$ ending at $2D$, and 80 grid points are placed in the azimuth. The suitability of these parameters has been established by Tinney et al. (2008a).

The pressure in the near irrotational field is measured using a combination of an azimuthal and a linear array (see Fig. 2b). The uniform azimuthal array has 16 sensors with their tips placed at $x = 3$ and $r = 1.5$. The linear array has 4 sensors at $x = 2.5, 3.0, 3.5$, and 4.0 on a meridional plane

with their tips forming a line inclined at 8.6° to the jet axis; the second sensor is actually common with the azimuthal array. All 19 sensors are 1/4 in. B&K 4939 microphones paired with B&K 2670 pre-amplifiers. The microphone signals are band-pass filtered between 20 Hz and 100 kHz and amplified by B&K 2690 amplifiers before being *simultaneously* acquired using National Instruments A/D boards and LabView software. Blocks of data are collected at 100 kHz with 4,096 data points per block, resulting in a spectral resolution of 24.4 Hz.

The auxiliary triggering capabilities of DaVis are used to ensure that each PIV snapshot is taken approximately in the middle of each pressure data block for computation of the cross-spectra. The Q-switch trigger signal for the laser is acquired simultaneously with the pressure so that the relative temporal location of the snapshot can be pin-pointed for each block in post-processing. The LAFPAs are triggered by a rectangular pulse train with very low on-percentage, which complicates the determination of phase from digital samples. Instead, the control signal for the first LAPFA is also fed to an Agilent 3320A 20 MHz waveform generator where each rising edge triggers a ramp signal. The signal thus derived is acquired simultaneously with the pressure and decoded in post-processing to infer the phase.

Additionally, 2-component PIV is performed on a meridional plane for the unforced jet and the jet forced at $St_{DF} = 0.3$, $m_F = 0$. This reuses much of the equipment and processing described above; the setup is depicted in Fig. 2a. The resulting vector map has spatial resolution of $0.093D$ and covers the entire jet plume over the axial domain between 0.3 and $12D$. For ensemble-averaged statistics, 1,000 image pairs are recorded at about 5 Hz. In addition, sets of 250 image pairs locked to 8 equally-spaced phases of the actuation signal are acquired for the forced case.

4 Results for unforced jet ROM

The axial domain of the ROM is in the range $5 \leq x \leq 7.75$, that is spanned by the cross-stream PIV sections. The model aims to capture the essential changes in the jet dynamics due to forcing in real time. For this, the domain must be just long enough to contain the largest of the relevant convecting coherent structures. The axial wavelength of structures generated by forcing near the JCM is $\sim 2D$ in the above axial range (see below and Kearney-Fischer et al. (2009)). Lengthening the axial domain makes reduced-order modeling more difficult since the POD modes converge more slowly (Kastner et al. 2009). This justifies the choice of the axial extent of the domain. Furthermore, setting the upstream limit of the domain at $x = 5$ is necessitated by the need to encompass the end of the potential core at $x \approx 6$. Although not pursued in this article, this is relevant for modeling the dominant noise sources (Hileman et al. 2005).

4.1 Stochastic estimation

The modeling process begins with the construction of an ensemble of approximate flow-field snapshots from experimental data using SLSE. Tinney et al. (2008b) developed this technique and applied it to the experimental data from a Mach 0.85 cold jet. Subsequently, Sinha et al. (2010b) have evaluated various configurations of pressure measurement and strategies for velocity pre-processing using the DNS data of Freund (2001). The procedure established therein is employed in the present work; hence, the details are omitted. The following discussion focuses on the assessment of the fidelity of reconstruction.

The velocity field was acquired as snapshots on cross-stream slices. Denoting the corresponding reconstructed field as $\mathbf{u}^{\mathrm{rec}}$, the following reconstruction fidelity metrics are proposed

$$\hat{\mathcal{A}}_i^{\mathrm{rec}}(x,m) := \frac{E\left[\langle \hat{u}_i^{\mathrm{rec}}, \hat{u}_i \rangle_{\hat{\Omega}_{x,m}}\right]_t}{\sqrt{E\left[\|\hat{u}_i^{\mathrm{rec}}\|_{\hat{\Omega}_{x,m}}^2\right]_t E\left[\|\hat{u}_i\|_{\hat{\Omega}_{x,m}}^2\right]_t}},$$

$$\hat{\varrho}_i^{\mathrm{rec}}(x,m) := \frac{E\left[\|\hat{u}_i^{\mathrm{rec}}\|_{\hat{\Omega}_{x,m}}^2\right]_t}{E\left[\|\hat{u}_i\|_{\hat{\Omega}_{x,m}}^2\right]_t}. \tag{5}$$

The first metric represents the alignment of the reconstructed field with the measured one for a particular component $i \in \{x, r, \theta\}$ and an x–m pair. The second is the ratio of the reconstructed energy to the measured energy.

The alignment metric is presented for the axial component of velocity in Fig. 3a. SLSE is biased toward larger scales that are better correlated, and this is evident in the improved accuracy at lower azimuthal mode numbers. Reconstruction fidelity is also seen to reduce with downstream distance owing to diminishing correlations with the fixed pressure sensing rig at the upstream location. Overall, the SLSE-reconstructed field appears to be approximating the larger scales quite adequately, and this is borne out by subsequent results.

The energy ratio metric presented in Fig. 3b highlights the fact that, without further modification, the derived POD modes would be biased toward lower values of m and x. Moreover, the modal energies from the empirical data enter into the ROM through the eddy viscosity (see the Appendix—Sect. 7.2), and their incorrect approximation would destabilize the ROM. Thus, the following ad hoc energy-scaling transformation is proposed to revert the energy of the estimated field to that found in the PIV

$$\hat{u}_i^{\mathrm{rec}}(x,r,t;m) \rightarrow \hat{u}_i^{\mathrm{rec}}(x,r,t;m)/\sqrt{\hat{\varrho}_i^{\mathrm{rec}}(x,m)}. \tag{6}$$

This is applied to the database of approximate snapshots for all the results presented here, since the ROMs performed much worse otherwise.
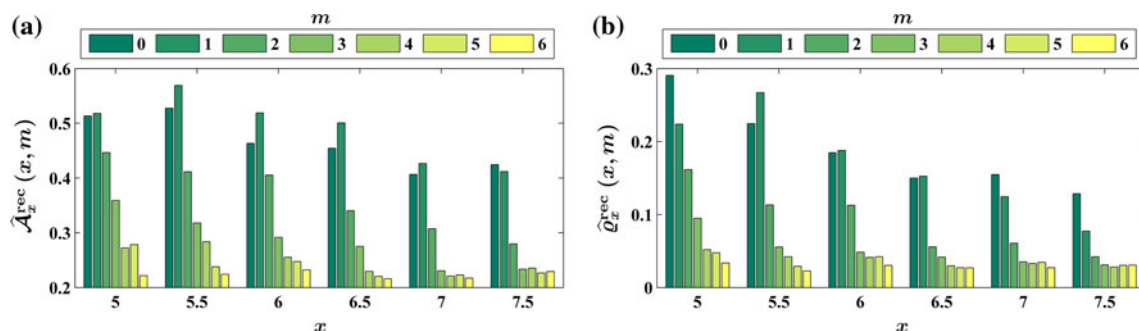

Fig. 3 Axial components of local modal SLSE reconstruction fidelity metrics. **a** Reconstruction alignment, **b** reconstruction energy

4.2 Proper orthogonal decomposition

The PIV measurements are performed with $\Delta x = 0.25$, but the SLSE-reconstructed approximate snapshots are interpolated on a grid with $\Delta x = 0.0625$. The centerline is avoided since it is a singularity for the cylindrical coordinate system, and the radial domain starts from $r = 0.0625$ instead. POD is performed on 700 independent snapshots, and the eigenspectrum is shown in Fig. 4. For $m \neq 0$, the eigenvalues are doubled to account for the negative modes. The eigenvalues are expressed as a percentage of the total energy measured in PIV (integrated over its corresponding coarser axial grid). Previous slice-POD results have indicated that, although $m = 3$ or 4 is the most energetic azimuthal mode at $x = 5$, the spectrum shifts to lower m's by $x = 8$ (e.g., Tinney et al. 2008a). The POD here integrates over this axial domain, and Fig. 4 demonstrates the dominance of $m = 1$. The paired energetic modes in $m = 1$ and 2 indicate a wave-like character in these modes. The 34
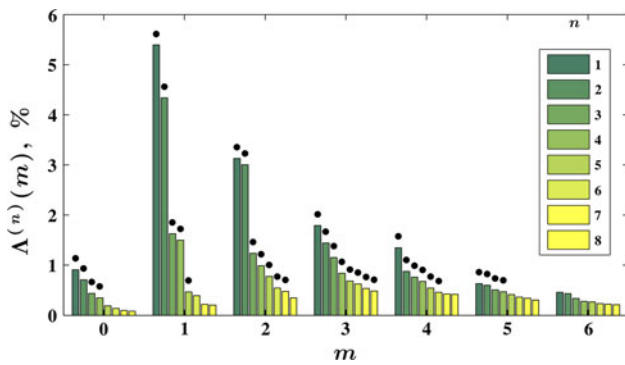

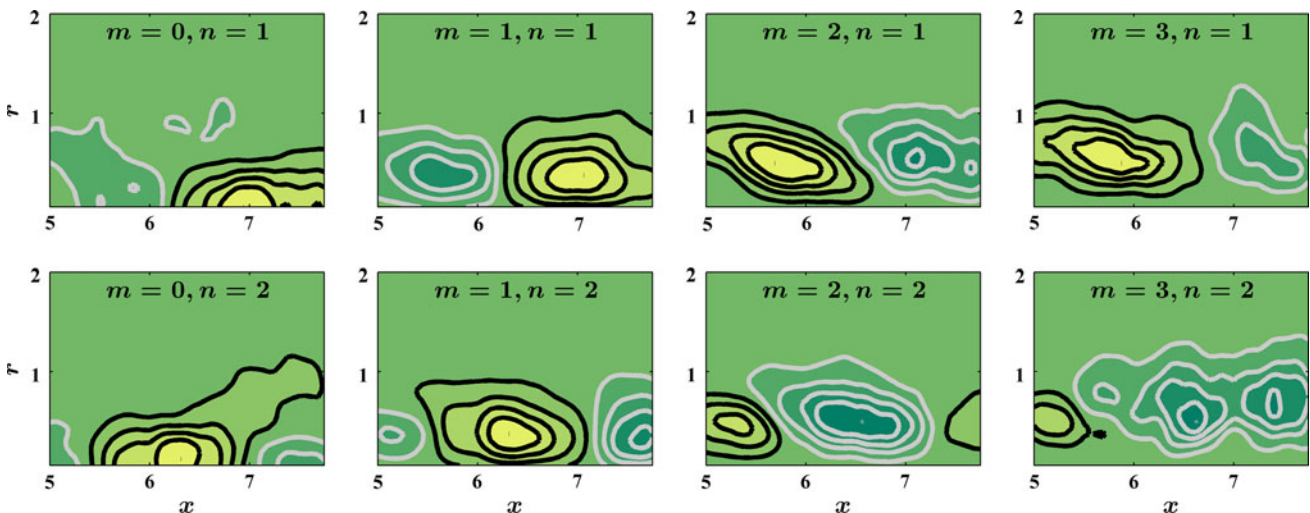**Fig. 4** Eigenspectrum with modes selected for the 35-D ROM indicated by *dots*

most energetic modes are indicated by dots and constitute 41 % of the fluctuation energy; these are used subsequently in the ROM. The high turbulence level is responsible for the slow convergence of POD modal energy.

The first few POD eigenfunctions of the axial component of velocity are examined in Fig. 5. The phase-shifted structure of the first pair of POD modes in $m = 1$ and 2 is readily observable. With increasing azimuthal mode, the locus of energy shifts from the high-speed side of the shear layer to the low-speed side (Tinney et al. 2008a), and this is demonstrated here too. Note that, without the transformation in Eq. 6, the structures at downstream locations would have much poorer resolution.

According to Noack et al. (2010), a "shift mode" encapsulates the primary mean flow dynamics, and its inclusion is crucial for stability and fidelity of the ROM. The model developed herein is designed to simulate forcing around the JCM. Thus, one candidate for the shift mode is the difference in the mean velocity fields obtained without forcing and with forcing near the JCM in experiments. The axial component of this differential mean velocity field is shown in Fig. 6. The potential core is shortened and the shear layer is spread due to forcing.

The unforced flow is axisymmetric in the mean. Moreover, in the forcing regime under consideration, all LAF-PA's are operated in phase to simulate axisymmetric forcing. Thus, the shift mode is an $m = 0$ mode. To include it in the ROMs, Gram–Schmidt orthonormalization is applied to all $m = 0$ POD modes, with the shift mode as the first vector field. Since the Fourier azimuthal modes of velocity are mutually orthogonal, the $m \neq 0$ modes are not affected by this inclusion. The shift mode accounts for 0.2 % of the flow energy; in comparison, the first POD mode in $m = 0$ captures 1.0 % of the energy (see Fig. 4).
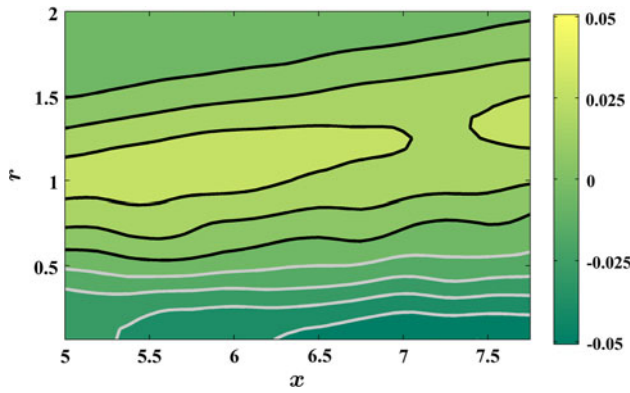

Fig. 5 First few $\hat{\Phi}_x$ modes. *Contour levels* are equi-spaced but arbitrary in absolute value. *Positive* and *negative* levels are *black* and *gray* respectively, but the sign is again arbitrary

Fig. 6 The mean axial velocities with forcing at $St_{DF} = 0.3$, $m_F = 0$ minus that from the unforced case, proposed as the shift mode

The inclusion of the shift mode is indeed found to stabilize the otherwise unstable ROMs. As a result, the trajectories remain bounded in simulations up to 5,000 flow time steps from 40 arbitrary initial conditions for ROMs of various dimensions from 15 to 40.

4.3 Reduced-order model

The accuracy of ROMs obtained through POD and Galerkin projection is not a monotonic function of the total energy of the retained modes (e.g., Rowley 2002; Ilak and

Rowley 2008). Indeed, for the present flow, the ROM built using the 35 most energetic modes out-performed the 25- and 45-D ROM's in terms of the metrics defined below. Hence, the 35-D ROM will be studied exclusively herein. The 35 most energetic modes are those indicated in Fig. 4 plus the shift mode. The values of N_m for the 35-D ROM can be read off from the figure; for example, $N_2 = 7$. Moreover, the highest azimuthal mode retained is $M = 5$.

The reduced-order modeling strategy outlined in Sect. 2 has been validated for the low-Re DNS database that consisted of time-resolved flow information (Sinha et al. 2010b). Such data are not available from experiments directly, but SLSE applied on the time-resolved pressure measurements is used to approximate a similar database. The azimuthal component of instantaneous vorticity (denoted as ω_θ) is used to visualize the structures. The first row of Fig. 7 depicts snapshots from the reconstructed database at four successive time instants after $t = \tau$, an arbitrary instant in the pressure record. The low-dimensional representations of these fields shown in the middle row are obtained by projection onto the 35-D subspace. The 35-D ROM is simulated using Runge–Kutta (4, 5) method, the initial condition being the projected field at $t = \tau$. The resulting ω_θ fields are presented at the corresponding times in the bottom row. The simulated field is found to track the projected field, with the size and
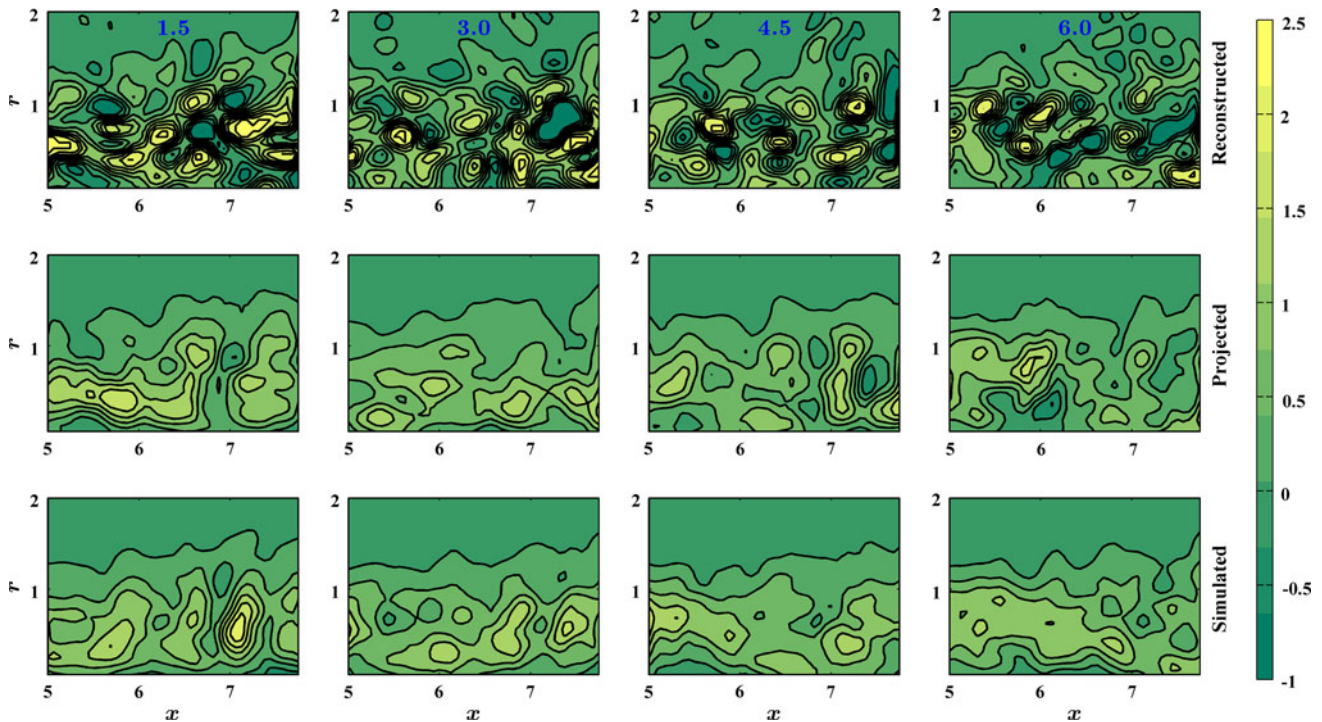

Fig. 7 Snapshots of simulated azimuthal vorticity on the $\theta = 0$ plane obtained from the 35-D ROM compared with the SLSE-reconstructed field as well as its projection on the 35-D POD basis at corresponding

times. The *times* of each snapshot from the initiation of simulation are indicated at the *top* of each *column*. The fields in the *top row* are saturated at the indicated levels to aid visual comparison

convection speed of the large-scale structures being reproduced well for several flow time steps beyond initiation of simulation.

Denoting the simulated velocity field by $\mathbf{u}^{\text{sim}}$, the following metrics are defined for quantifying the fidelity of ROMs:

$$\mathcal{E}^{\text{sim}}(T) := \frac{E\left[\|\mathbf{u}^{\text{sim}}(\tau + T) - \mathcal{P}_S\mathbf{u}(\tau + T)\|^2_{\Omega}\right]_{\tau}}{E\left[\|\mathcal{P}_s\mathbf{u}(t)\|^2_{\Omega}\right]_t}, \quad (7a)$$

$$\mathcal{A}^{\text{sim}}(T) := E\left[\frac{\langle \mathbf{u}^{\text{sim}}(\tau + T), \mathcal{P}_S\mathbf{u}(\tau + T)\rangle_{\Omega}}{\|\mathcal{P}_S\mathbf{u}(\tau + T)\|_{\Omega}\|\mathbf{u}^{\text{sim}}(\tau + T)\|_{\Omega}}\right]_{\tau}. \quad (7b)$$

Here, T refers to the time from initiation of model simulation, and the expectation is over different initiation instants τ. Recall that $\mathcal{P}_S\mathbf{u}$ denotes the projection of the velocity field $\mathbf{u}$ (reconstructed from SLSE) onto the subspace S used to construct the ROM. The first metric represents the normalized mean square error in the simulated field compared with the projected one. The second metric measures the alignment of the simulated field with the projected field and signifies fidelity in reproduction of the large-scale structure dynamics.

Figure 8 presents the two metrics evaluated by averaging over simulations from 20 independent initial conditions, denoted in the definition by $t = \tau$. The bars depict the ± 1SD (over the different initial conditions) at representative times. Although rapid degradation is observed immediately after initiation, significant alignment can be seen up to ~2 flow time steps from initiation. The simulation error reaches unity at $T \approx 0.6$.

Statistical analysis is performed on trajectories obtained by simulating the ROM up to 1,000 flow time steps from 50 different initial conditions. The projected POD coefficient corresponding to the shift mode has vanishing mean over sufficiently large ensembles. However, the corresponding mean from simulations is always found to be finite. It is hypothesized that the truncation of the eigenfunction basis is not fully counteracted by the eddy viscosity model,
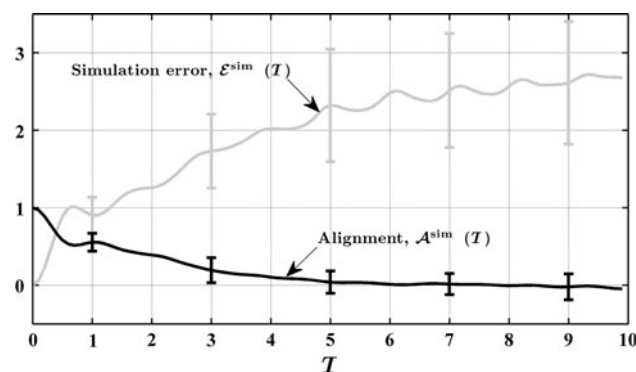
resulting in this modification of the mean location of the flow attractor in phase–space.

Figure 9 presents the mean square of the axial fluctuating velocity field from the simulation at the centerline and lip-line. These fluctuations are with respect to the *simulated* mean field. Comparison with meridional PIV measurements reveal that the centerline statistics are very accurate. This is accounted for by the relative fidelity of the SLSE-reconstructed $m = 0$ field (see Fig. 3a), which dominates the centerline as observed in Fig. 5. The lip-line energy is substantially overpredicted by the ROM, presumably because of inaccurate modeling of the higher azimuthal modes that are active here. ROMs of dimensionality lower and higher demonstrated poorer fidelity in this comparison.

Further insight is afforded by a study of the azimuthal modal content of the simulated field in Fig. 10. Compared with cross-stream PIV data, the lower m's are seen to be modeled with sufficient accuracy. However, energies at downstream stations and higher m's are increasingly overpredicted. This is a disadvantage of the scaling performed in Eq. 6 to improve model fidelity. The truncation of the spatial basis creates a barrier in the energy cascade
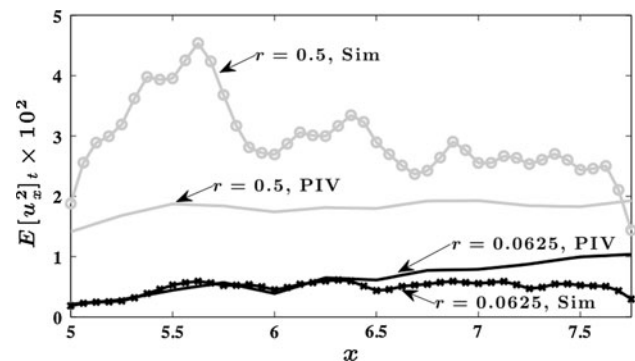
Fig. 9 Local energies of u_x from experiments and ROM near *centerline* and *lipline*

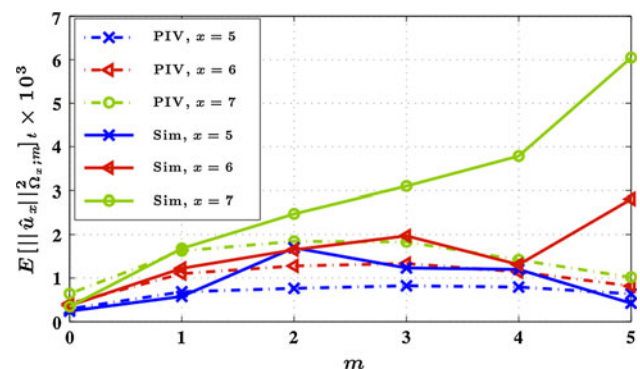**Fig. 8** Simulation fidelity metrics for 35-D ROM

Fig. 10 Radially integrated azimuthal modal energies of u_x from experiments and ROM at three axial stations
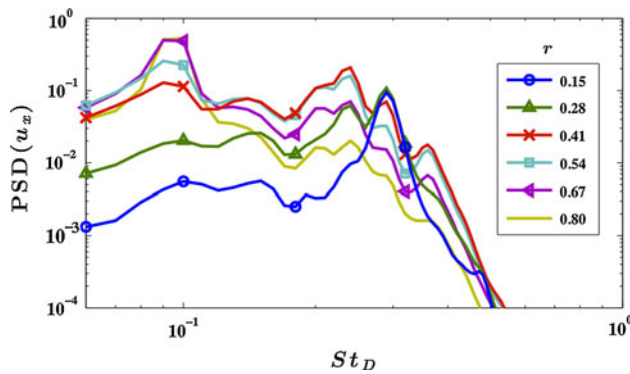
Fig. 11 PSD of u_x at $x = 6$ from ROM

causing a "pile-up," which may also explain the increase in energy with m.

The frequency domain character of the ROM is important for reproducing the response of the jet to periodic excitation, prompting the study of its power spectral density (PSD) in Fig. 11. The low-frequency parts of the spectra are flat, indicating simulation of broadband turbulence. The high-frequency roll-off rates are steeper than the turbulent inertial subrange owing to the absence of the smaller scales in the ROM. The jet preferred mode (Petersen and Samet 1988) is captured in the sharp peak at $St_D \approx 0.3$ near the centerline, although its relative amplitude appears to be overpredicted (refer to Tinney et al. (2006) for a comparison). In moving radially outward, the spectral levels first increase and then decrease beyond the lip-line, as reported in the literature (Tinney et al. 2006). Finally, the shoulder-frequency starts off high near the centerline, but reduces in traversing outward.

The statistics presented above from the long-time simulations of the ROM obtained from experimental data are quite encouraging. They indicate that the essential dynamics of the jet are being captured with sufficient fidelity in spite of the many simplifying assumptions.

5 Incorporating the effect of LAFPAs in the ROM

Detailed modeling of the plasma actuation is very difficult due to the paucity of measurements in the challenging experimental environment as well as the complexity of the physics and the wide separation of scales. The available observations were used to inform a quasi-1D arc filament model in quiescent conditions (Utkin et al. 2007). It predicted a rapid diminution of the initial thermal effect but a much longer persistence of the generated compressive pulse. Compression waves have indeed been observed in schlieren imaging (Hahn et al. 2011) and near-field pressure signals (Sinha et al. 2010a) in the forced jet. This justifies the neglect of thermal effects of actuation at the downstream modeling

domain. Instead, the model presented below incorporates the actuation effect in the ROM within the constraints of the necessary incompressible assumption.

5.1 Phenomenological model of LAFPA forcing

A study of the proposed ROM in Eq. 4 reveals that, once the unforced jet has been modeled, actuation effects may be incorporated in two main ways. The coefficients of the ROM may have to be modified if the POD basis is unsuitable for capturing the forced velocity fields. Otherwise, the pressure at the ends of the modeling domain (see Fig. 1) may incorporate the forcing information. A combination of the two effects may also prevail.

The effect of actuation may fundamentally alter the model of the unforced flow by rendering irrelevant the POD basis derived thereof. Empirical data for the POD must then be collected and merged from several open-loop forcing experiments covering the range of interest (e.g., Caraballo et al. 2008). This is mostly an issue if very few ($\lesssim 10$) modes are retained in the ROM and may cease to matter when more modes are included for simulating broadband fluctuations. The following describes a technique for rudimentary assessment of axisymmetric ($m_F = 0$) forcing effects on the POD basis functions.

Two-component PIV has been performed in the meridional plane for the unforced jet as well as for the jet forced near the JCM ($St_{DF} = 0.3$, $m_F = 0$). A very crude approximation of the $m = 0$ mode of axial velocity fluctuations may be obtained by averaging the fluctuations from the two sides of the centerline in any snapshot. The mean velocity from the unforced jet data is used in the Reynolds decomposition of both unforced and forced jet data. The POD for the forced jet is performed in the standard manner. For the unforced jet, the shift mode computed with the forcing case is included as before. Half of the forced jet field snapshots form the input for POD, and the remaining are used for assessing the reconstruction fidelity. The energy of residual error in POD reconstruction is determined for increasing number of POD basis functions, N_0. In each case, the reconstruction is also performed using the POD basis from the unforced case. The difference in the energy of the reconstruction error is found to be less than 2.2 % of the total fluctuation energy for $N_0 \in [1, 10]$. Consequently, the effect of actuation near the JCM *cannot* be incorporated in the ROM through a modification of the coefficients linked to a changing POD basis.

Instead, it is proposed to model the pressure fluctuations at the inflow and outflow boundaries of the modeling domain by a deterministic function of the forcing parameters. We have noted in the introduction to this section that the plasma actuation indeed manifests as a periodic compressive pulse at downstream stations, with minimal thermal modification. A

phase-resolved description of the velocity fluctuations on the relevant cross-sections is available from experiments with forcing near the JCM. Additionally, an LES of this forcing case (albeit for a Mach 1.3 jet) is also available from Gaitonde and Samimy (2011). A technique is presented below to employ these building blocks to arrive at the desired functional relation for the pressure.

Lau et al. (1972) showed that a local phase relation exists between the hydrodynamic pressure and the axial and radial velocity in a low-Re jet owing to the presence of large-scale vortical structures in the mixing layer. Pressure fluctuations are in phase with axial velocity fluctuations in the entrainment region, whereas they are in anti-phase in the core region. Within the mixing layer, the correlation switches sign. Pressure fluctuations are in quadrature with, and lead, the radial velocity fluctuations in all three regions. Numerous experiments have established that quasi-periodic large-scale vortical structures also exist in a high-Re jet forced with LAFPAs near the JCM (e.g., Samimy et al. 2007a; Kearney-Fischer et al. 2009). Thus, the phase of the periodic part of the hydrodynamic pressure can be determined from knowledge of the phase-resolved velocity fluctuations at the same position.

The vortex model is insufficient for determining the amplitude of the pressure field, and thus use is made of the JCM forcing case from the LES database. Figure 12a–c demonstrate that the phase relations, as captured in the relevant cross-correlations from the LES data, agree closely with the vortex model. The correlation coefficients are highly periodic, and the amplitudes are almost unity, due to the generation of periodic coherent vortices that dominate the hydrodynamic field. In experiments, although the PIV snapshots are at uncorrelated times, the simultaneous acquisition of the actuation phase allows the computation of the phase-resolved velocity correlations shown in Fig. 12d. The contour map is similar to its time-resolved counterpart observed for the LES data in Fig. 12c, in spite of the large difference in Mach numbers. The strength of these correlations again demonstrates the degree of organization attained with LAFPA forcing near the JCM for the high-Re jet.

The pressure–velocity correlations in the LES data will be employed to estimate the pressure field at the inflow and outflow boundaries of the ROM for experimental data. Ideally, one would prefer to use both axial and radial velocity components in the estimation, owing to the joint
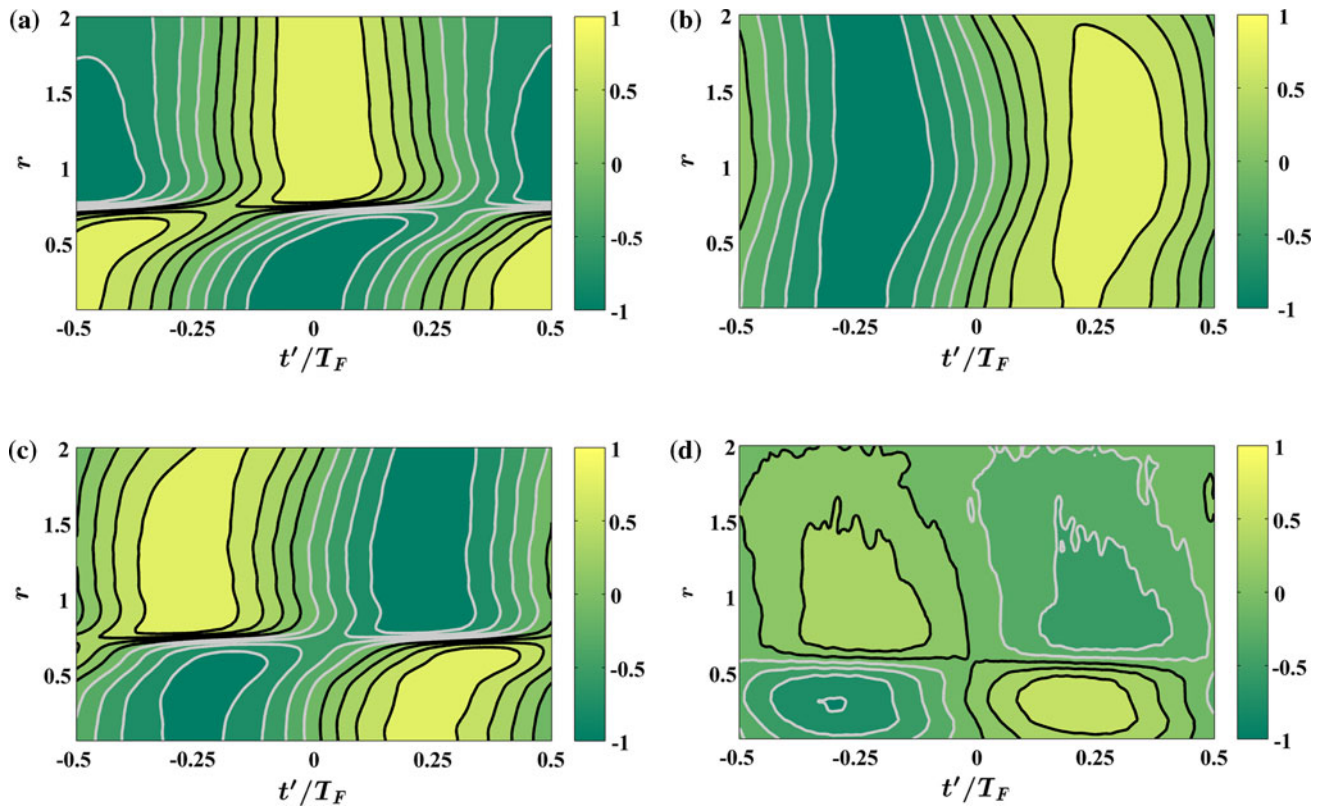

Fig. 12 Computational and experimental cross-correlation coefficients of $m = 0$ mode of pressure and velocity at $x = 5$ for forcing with $St_{DF} = 0.3$, $m_F = 0$. Here, σ denotes the root mean square at a specified x and r, and T_F ($= 1 / St_{DF}$) is the forcing period. **a** $E\left[\hat{u}_x^H(t + t')\hat{p}(t)\right]_t/(\sigma_{\hat{u}_x}\sigma_{\hat{p}})$ from LES. **b** $E\left[\hat{u}_r^H(t + t')\hat{p}(t)\right]_t/(\sigma_{\hat{u}_r}\sigma_{\hat{p}})$ from LES, **c** $E\left[\hat{u}_x^H(t + t')\hat{u}_r(t)\right]_t/(\sigma_{\hat{u}_x}\sigma_{\hat{u}_r})$ from LES, **d** $E\left[\hat{u}_x^H(t + t')\hat{u}_r(t)\right]_t/(\sigma_{\hat{u}_x}\sigma_{\hat{u}_r})$ from experiment

correlations. However, detailed comparison of the radial variations of the $u_x - u_r$ correlation profiles in Fig. 12c, d reveals certain differences. The reason can be traced to differences in the location of the axial station relative to the end of the potential core, the precise jet width, as well as the typical center of the passing vortices. The $u_x - p$ correlations switch sign within the mixing layer, and mismatches in the position of this switch introduces errors in the estimate. On the other hand, the $u_r - p$ correlations maintain a uniform phase relation throughout the radial domain.

The foregoing discussion motivates the following estimation model:

$$\hat{p}(x, r, t; m_F)$$
$$\approx \frac{1}{T_F} \int_{-T_F/2}^{T_F/2} \hat{L}^{\mathrm{H}}(t'; x, r, m_F) \hat{u}_r(x, r, t + t'; m_F) \mathrm{d}t', \qquad (8)$$

where the coefficients $\hat{L}$ remain to be determined. Only the pressure field in $m = m_F$ is assumed to be organized enough to be modeled in this fashion. Moreover, the periodicity imposed by LAFPA forcing is exploited to limit the time-dependency horizon. This is recognized as a linear stochastic estimation problem with finite time delays.

The temporal periodicity of the model implies that the solution is more efficient in Fourier space, so that the spectral variant (Tinney et al. 2006) is actually invoked for determining $\hat{L}$. Indeed, only the fundamental and the first harmonic of the forcing frequency are sufficient, and these are used for the approximation shown in Fig. 13a. The radial and temporal variation of the pressure field obtained directly from LES in Fig. 13b is quite comparable. The absolute amplitude is about 2.5 times higher in the LES, but this can be explained in part by the increased Mach number. Indeed, a virtual pressure probe placed at the same location in the computational domain as the azimuthal microphone array in experiments measured an amplitude about twice that observed in experiments.

This completes the approximation of the pressure field at $x = 5$, the inflow plane for the model. The outflow plane at $x = 7.75$ has not been discussed. Both the phase-averaged u_r fluctuations in experiments and the pressure fluctuations in LES are much reduced at this station and so are profitably neglected. Thus, the approximate axisymmetric pressure field presented in Fig. 13a is adequate for computing the "forcing term" in the ROM of Eq. 4.

The LAFPA model has been developed from empirical data (both experimental and numerical) of the jet forced at $St_{DF} = 0.3$, $m_F = 0$ exclusively. However, the validity of the model is expected to extend to a neighborhood of the parameter space. In particular, the phase variations of the pressure term can be imposed over varying forcing periods to simulate different St_{DF}'s, and this is pursued in the following. Extension of the above pressure pattern to other m_F's may be more difficult, but the modeling technique described here can be easily reused with appropriate empirical data.

5.2 Validating the model of the forced jet

The 35-D ROM is simulated with forcing at $St_{DF} = 0.3$, $m_F = 0$ over 75 forcing periods starting from 20 different initial conditions of the unforced jet. The first 25 forcing periods are neglected in the computation of statistics. Note that the trajectories did not diverge in simulations over 5,000 flow time steps. A triple decomposition (Reynolds and Hussain 1972) is performed on the simulated velocity field, and the axisymmetric mode of the phase-averaged velocity field is denoted by $\tilde{\mathbf{U}}$. The azimuthal component of vorticity computed from this field ($\tilde{\omega}_\theta$) is presented in Fig. 14a for an arbitrary phase. For comparison, the corresponding field from phase-locked meridional PIV is shown in Fig. 14b. The shapes and intensities of the structures match quite closely, although the wavelength is somewhat under-predicted (to be quantified below).
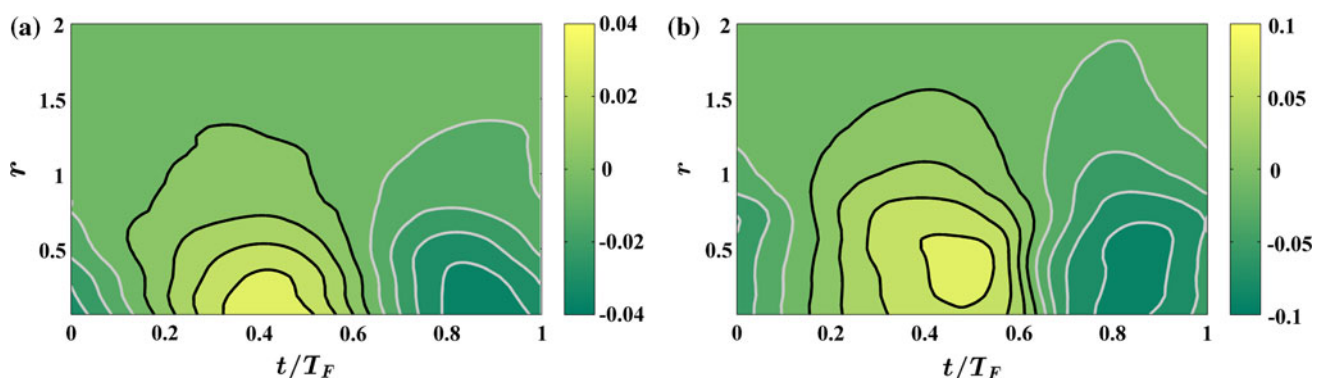

Fig. 13 Experimental and computational phase-resolved $m = 0$ pressure field at $x = 5$ for forcing at $St_{DF} = 0.3$, $m_F = 0$. **a** Estimated from experiments, **b** directly from LES. Note that the *color-scales* are different
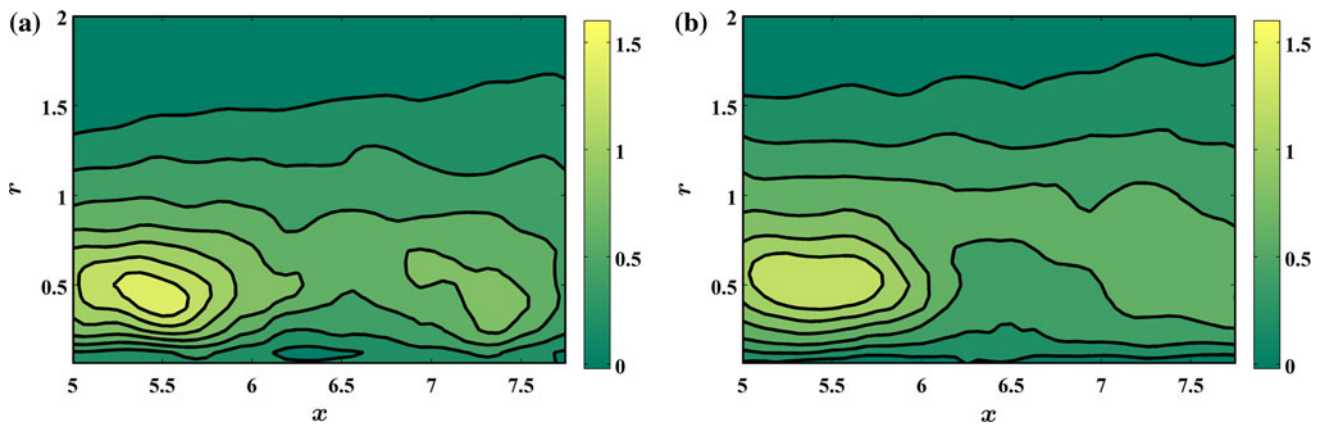
Fig. 14 Phase-averaged azimuthal vorticity with forcing at $St_{DF} = 0.3$, $m_F = 0$. **a** From stimulation of 35-D ROM, **b** from phase-locked PIV in experiments

The vorticity contours presented in Fig. 14 aid in visualization of structures, but $\tilde{\mathbf{u}} = \tilde{\mathbf{U}} - E[\tilde{\mathbf{U}}]_t$ being numerically more accurate, are used in quantitative comparisons of the phase-averaged structure pattern now. The wavelength is calculated from the axial separation of the peaks of the $\tilde{u}_x$ auto-correlation (in x) at the centerline. Sixteen equally spaced phases are extracted from the simulated data, and the average wavelength is reported in Table 1. As described in the previous section, the phenomenological LAFPA model is simulated over a range of St_{DF}'s in a neighborhood of the JCM. Per our expectation, the wavelength decreases monotonically with increasing St_{DF}. Phase-resolved three-component PIV at $x = 5, 6$, and 7 is used to estimate the wavelength in experiments from phase lags of the cross-correlations. The ROM under-predicts the wavelengths as well as the sharpness of the decrease. Apart from the shift mode, only four other $m = 0$ POD modes are included in the ROM, which explains the limited range of wavelengths that can be represented. Moreover, the axial extent of the domain, being 2.75 D, may also be contributing to the discrepancy.

The amplitude of the wave pattern in the $\tilde{\mathbf{u}}$ field is computed by extracting the fundamental from a Fourier transform in phase. As presented in Table 1, the ROM predicts a strong response at $St_{DF} = 0.3$, and the much reduced response at side St_{DF}'s is indicative of resonance. This is explained by the spectral peak at $St_D = 0.3$ exhibited by the ROM of the unforced jet in Fig. 11. Comparison with the corresponding amplitudes calculated from experiments validates the optimal response behavior. However, the strength of the response is under-predicted, and the sharpness is overpredicted.

Figure 14 has depicted $\tilde{\omega}_\theta$ for a particular phase. The peak absolute value appearing within the modeling domain across all sixteen extracted phases is presented in Table 1 for the different St_{DF}'s. The variation of vorticity magnitude with St_{DF} is of direct interest for mixing enhancement.

Table 1 Quantitative results of $m_F = 0$ mode forcing in 35-D ROM and experiments

Metric	Source	Forcing Strouhal number, St_{DF}				
		0.20	0.25	0.30	0.35	0.40
Wavelength[a]	ROM	2.41	2.18	2.09	2.05	1.98
	Experiment	–	3.08	2.54	2.20	–
Amplitude[b] $\times 10$	ROM	0.13	0.32	0.85	0.23	0.13
	Experiment	–	1.11	1.40	1.31	–
Azimuthal vorticity[c]	ROM	1.24	1.32	1.54	1.30	1.27
	Experiment	–	–	1.48	–	–
Pressure[d] $\times 1,000$	Experiment	3.29	3.85	4.11	3.65	2.71
TKE[e] $\times 100$	ROM	0.99	1.07	1.45	0.99	1.03
	Experiment	–	–	1.33	–	–

[a] From $\tilde{u}_x$ at $r = 0.0625$, normalized by D

[b] From $\tilde{u}_x$ at $x = 6$ and $r = 0.0625$, normalized by U_j

[c] Peak value of $\tilde{\omega}_\theta$, normalized by U_j /D

[d] Root mean square of $m = 0$ mode in the near field at $x = 3$, $r = 1.5$

[e] Averaged over $x \in [5, 7.75]$ at $r = 0.0625$, using u_x and u_r

The ROM is predicting that the maximum effectiveness of forcing should occur in a narrow region of the forcing parameter space near the JCM. This mirrors the $\tilde{u}_x$ amplitude variations and has the same explanation. The peak $\tilde{\omega}_\theta$ observed within the relevant domain in phase-locked PIV at $St_{DF} = 0.3$ is also noted in the table. The agreement with the predictions from the ROM is very good, given the modeling simplifications.

The hydrodynamic pressure in the near-field filters out the smaller scales and thus provides a low-dimensional description of the mixing layer fluctuations. The pressure field has been extensively surveyed using the sensing rig described in Sect. 3 and also discussed in depth by Sinha et al. (2010a). The variation in the axisymmetric ($m = 0$) mode of pressure reported in Table 1 reflects the optimal

response of the jet to forcing near the JCM and provides useful validation for the 35-D ROM.

The centerline TKE has been used in the literature to characterize mixing enhancement (e.g., Samimy et al. 2010). Figure 9 has demonstrated that the ROM is able to reproduce the centerline turbulent fluctuations in the unforced jet quite closely. Table 1 presents the 2-component centerline TKE (averaged over the axial domain of the ROM) for several St_{DF}'s. The corresponding value from experiments at $St_{DF} = 0.3$ does not represent a large discrepancy. Similar to the wave amplitude and vorticity metrics, the ROM predicts an optimal TKE for forcing near the JCM.

6 Conclusions

Plasma actuation of high-speed and high Reynolds number jets near the JCM frequency generates robust coherent structures which has application in mixing enhancement. The present article describes the design of a feedback-oriented empirical reduced-order model for this flow.

Stochastic estimation, POD, and Galerkin projection are used in sequence to model the unforced jet from experimental data. The inclusion of a specially designed "shift mode," encoding the dominant flow change between the unforced state and the state of JCM forcing, stabilizes the ROM. A detailed analysis is presented for the performance of a 35-D model of the jet flow field near the end of the potential core. It is compared with the acquired experimental data as well as an approximation of time-resolved data derived thereof. Feedback controllers sense the system state in real time, thereby effectively shortening the required prediction horizon. The ROM provides useful predictions over the first few flow time step after initiation, beyond which simulated trajectories quickly diverge from the actual. Since the plasma actuators are frequency modulated, the long-term ensemble-averaged and spectral statistics predicted by the ROM are also important. In these respects, the model demonstrates sufficient accuracy. Overall, the spectrum has the broadband character typically measured in experiments. Due to its low dimensionality, the ROM spectrum exhibits a strong peak at the preferred mode, a diminished version of which is commonly observed in reality. The fluctuation energies in the lower azimuthal modes as well as along the centerline are accurately replicated.

The effect of plasma actuation is incorporated in the ROM through a deterministic shaping of the pressure field at the upstream boundary of the cylindrical modeling domain. The pressure function is obtained using stochastic estimation in conjunction with experimental measurements and an existing numerical simulation database. This phenomenological model of the pressure is designed to be valid for axisymmetric forcing at frequencies in a neighborhood

of the JCM. Phase-averaged and ensemble-averaged statistics predicted by the ROM agree well with experimental observations for forcing near the JCM frequency. Moreover, the highly nonlinear response of the jet, as reflected by the narrow range of optimal forcing parameters for mixing enhancement, is also captured with sufficient accuracy.

Considered all together, the results suggest that the 35-D model for simulating LAFPA-induced mixing enhancement in high-Re jets may be adequate for feedback control design. The actual design of the feedback laws in this challenging problem remains an open question.

Appendix

Inner products

The Lebesgue space of square–integrable functions with domain in Ω is denoted by $\mathcal{L}_\Omega^2$. The appropriate inner product for physical vector fields in $\mathcal{L}_\Omega^2$ is

$$\langle \mathbf{v}, \mathbf{w} \rangle_\Omega := \int\limits_{X_1}^{X_2} \int\limits_0^R \int\limits_{-\pi}^{\pi} \mathbf{w}^T(x, r, \theta) \mathbf{v}(x, r, \theta) r \mathrm{d}\theta \mathrm{d}r \mathrm{d}x,$$
$$\mathbf{v}, \mathbf{w} \in \mathcal{L}_\Omega^2, \quad \mathbf{v}, \mathbf{w} : \Omega \to \mathbb{R}^3,$$

where $(\cdot)^T$ denotes transpose. The inner product for the mth azimuthal Fourier mode of a vector field in $\mathcal{L}_{\hat\Omega,m}^2$ is

$$\langle \hat{\mathbf{v}}, \hat{\mathbf{w}} \rangle_{\hat\Omega,m} := \int\limits_{X_1}^{X_2} \int\limits_0^R \hat{\mathbf{w}}^H(x, r; m) \hat{\mathbf{v}}(x, r; m) r \mathrm{d}r \mathrm{d}x,$$
$$\hat{\mathbf{v}}, \hat{\mathbf{w}} \in \mathcal{L}_{\hat\Omega,m}^2, \quad \hat{\mathbf{v}}, \hat{\mathbf{w}} : \hat\Omega \to \mathbb{C}^3.$$

If vector fields in the azimuthal Fourier space are defined at a single axial location only, say x, then the domain becomes $\hat\Omega_x := \{x\} \times [0, R]$, and one defines

$$\langle \hat{\mathbf{v}}, \hat{\mathbf{w}} \rangle_{\hat\Omega_x,m} := \int\limits_0^R \hat{\mathbf{w}}^H(x, r; m) \hat{\mathbf{v}}(x, r; m) r \mathrm{d}r, \quad \hat{\mathbf{v}}, \hat{\mathbf{w}} \in \mathcal{L}_{\hat\Omega_x,m}^2,$$
$$\hat{\mathbf{v}}, \hat{\mathbf{w}} : \hat\Omega \to \mathbb{C}^3.$$

These definitions can be readily modified to obtain the corresponding scalar inner products that address a single

component of the vector fields; the form of the arguments would make the notation unambiguous. Finally, the corresponding norms have the standard notation. For example, $\|\hat{\mathbf{v}}\|_{\hat{\Omega},m} := \sqrt{\langle \hat{\mathbf{v}}, \hat{\mathbf{v}} \rangle_{\hat{\Omega},m}}$.

Details of the ROM

The non-dimensionalized incompressible Navier–Stokes equation in generic coordinates is

$$\frac{\partial \mathbf{U}}{\partial t} = \frac{1}{Re}\nabla^2\mathbf{U} - (\mathbf{U}\cdot\nabla)\mathbf{U} - \nabla P$$

$$=: \frac{1}{Re}\mathcal{N}_L(\mathbf{U}) + \mathcal{N}_Q(\mathbf{U},\mathbf{U}) + \mathcal{N}_F(P).$$

Reynolds decomposition is applied to the velocity and pressure fields, followed by azimuthal Fourier decomposition and POD of the fluctuations. Subsequent Galerkin projection onto the retained azimuthal Fourier and POD basis yields the reduced-order model in Eq. 4. The static coefficients in Eq. 4 are

$$\mathcal{G}_C(n) := \left\langle \frac{1}{Re}\hat{\mathcal{N}}_L(\overline{\mathbf{U}}) + \hat{\mathcal{N}}_Q(\overline{\mathbf{U}},\overline{\mathbf{U}}) + \hat{\mathcal{N}}_F(\overline{\mathcal{P}}), \hat{\mathbf{\Phi}}^n \right\rangle_{\hat{\Omega},m=0},$$

$$\mathcal{G}_L(n, n', m) := \frac{1}{Re}\left\{1 + \delta_{n,n'}v_T^n(m)\right\}\mathcal{G}_L^{\mathrm{d}}(n, n', m) + \mathcal{G}_L^{\mathrm{c}}(n, n', m),$$

$$\mathcal{G}_L^{\mathrm{d}}(n, n', m) := \left\langle \hat{\mathcal{N}}_L\left(\hat{\mathbf{\Phi}}^{n'}\right), \hat{\mathbf{\Phi}}^n \right\rangle_{\hat{\Omega},m},$$

$$\mathcal{G}_L^{\mathrm{c}}(n, n', m) := \left\langle \hat{\mathcal{N}}_Q\left(\overline{\mathbf{U}}, \hat{\mathbf{\Phi}}^{n'}\right) + \hat{\mathcal{N}}_Q\left(\hat{\mathbf{\Phi}}^{n'}, \overline{\mathbf{U}}\right), \hat{\mathbf{\Phi}}^n \right\rangle_{\hat{\Omega},m},$$

$$\mathcal{G}_Q(n, n', n'', m, m') := \left\langle \hat{\mathcal{N}}_Q\left(\hat{\mathbf{\Phi}}^{n'}(m'), \hat{\mathbf{\Phi}}^{n''}(m-m')\right), \hat{\mathbf{\Phi}}^n \right\rangle_{\hat{\Omega},m}.$$

The accented operators $\hat{\mathcal{N}}$ refer to the azimuthal Fourier transforms of the corresponding physical operators $\mathcal{N}$, obtained by substituting $\partial/\partial\theta$ with im when the supplied argument has azimuthal mode m. Ensemble-average quantities are treated as $m = 0$ fields. All these coefficients are real following the symmetry arguments presented by Sinha et al. (2010b). The "forcing" term in Eq. 4 arises from $\langle \hat{\mathcal{N}}_F(\hat{p}(t)), \hat{\mathbf{\Phi}}^n \rangle_{\hat{\Omega},m}$ through an invocation of Gauss' divergence theorem, and an additional assumption that $\hat{\Phi}_r|_{r=R} \approx 0$.

Following Cazemier et al. (1998), the modal eddy viscosity factor is uniquely determined by requiring that the time derivative of modal energy should vanish in ensemble average:

$$v_T^n(m) = \max\left[0, -1 - \frac{Re}{\mathcal{G}_L^{\mathrm{d}}(n,n,m)\Lambda^n(m)}\left\{\mathcal{G}_L^{\mathrm{c}}(n,n,m)\Lambda^n(m)\right.\right.$$

$$+ \sum_{m'=m-M}^{M}\sum_{n'=1}^{N_{m'}}\sum_{n'=1}^{N_{m-m'}}\mathcal{G}_Q(n,n',n'',m,m')$$

$$\left.\left.E\left[\Re\left((\hat{\alpha}^n(m))^{\mathrm{H}}\hat{\alpha}^{n'}(m')\hat{\alpha}^{n''}(m-m')\right)\right]_t\right\}\right].$$

References

Aubry N, Holmes P, Lumley JL, Stone E (1988) The dynamics of coherent structures in the wall region of a turbulent boundary layer. J Fluid Mech 192:115–173

Caraballo E, Kasnakoglu C, Serrani A, Samimy M (2008) Control input separation methods for reduced-order model-based feedback flow control. AIAA J 46(9):2306–2322

Cazemier W, Verstappen RWCP, Veldman AEP (1998) Proper orthogonal decomposition and low-dimensional models for driven cavity flows. Phys Fluids 10(7):1685–1699

Crow S, Champagne F (1971) Orderly structure in jet turbulence. J Fluid Mech 48(3):547–591

Freund JB (2001) Noise sources in a low-Reynolds-number turbulent jet at Mach 09. J Fluid Mech 438(1):277–305

Gaitonde DV, Samimy M (2011) Coherent structures in plasma-actuator controlled supersonic jets: axisymmetric and mixed azimuthal modes. Phys Fluids 23:095104

Gloerfelt X (2008) Compressible proper orthogonal decomposition/Galerkin reduced-order model of self-sustained oscillations in a cavity. Phys Fluids 20:115105

Hahn C, Kearney-Fischer M, Samimy M (2011) On factors influencing arc filament plasma actuator performance in control of high speed jets. Exp Fluids 51:1591–1603

Hileman J, Thurow B, Caraballo E, Samimy M (2005) Large-scale structure evolution and sound emission in high-speed jets: real-time visualization with simultaneous acoustic measurements. J Fluid Mech 544:277–307

Ilak M, Rowley CR (2008) Modeling of transitional channel flow using balanced proper orthogonal decomposition. Phys Fluids 20:034103

Kastner J, Kim J-H, Samimy M (2009) A study of the correlation of large-scale structure dynamics and far-field radiated noise in an excited Mach 0.9 jet. Int J Aeroacoust 8(3):231–259

Kearney-Fischer M, Kim J-H, Samimy M (2009) Control of a high Reynolds number Mach 0.9 heated jet using plasma actuators. Phys Fluids 21(9):095101

Kerherve F, Jordan P, Cavalieri AVG, Delville J, Bogey C, Juve D (2012) Educing the source mechanism associated with downstream radiation in subsonic jets. J Fluid Mech 710:606–640

Lau JC, Fisher MJ, Fuchs HV (1972) The intrinsic structure of turbulent jets. J Sound Vib 22(4):379–406

Noack BR, Schlegel M, Morzynski M, Tadmor G (2010) System reduction strategy for Galerkin models of fluid flows. Int J Numer Meth Fluids 63:231–248

Petersen RA, Samet MM (1988) On the preferred mode of jet instability. J Fluid Mech 194:153–173

Rempfer D (2000) On low-dimensional Galerkin models for fluid flow. Theor Comput Fluid Dyn 14(2):75–88

Reynolds WC, Hussain AKMF (1972) The mechanics of an organized wave in turbulent shear flow. Part 3. Theoretical models and comparisons with experiments. J Fluid Mech 54(2):263–288

Rowley CR (2002) Modeling, simulation, and control of cavity flow oscillations. PhD thesis, California Institute of Technology

Rowley CR (2005) Model reduction for fluids, using balanced proper orthogonal decomposition. Int J Bifurcat Chaos 15(3):997–1013

Samimy M, Kim J-H, Kastner J, Adamovich I, Utkin Y (2007a) Active control of high-speed and high-Reynolds-number jets using plasma actuators. J Fluid Mech 578:305–330

Samimy M, Kim J-H, Kastner J, Adamovich I, Utkin Y (2007b) Active control of a Mach 0.9 jet for noise mitigation using plasma actuators. AIAA J 45(4):890–901

Samimy M, Kim J-H, Kearney-Fischer M, Sinha A (2010) Acoustic and flow fields of an excited high Reynolds number axisymmetric supersonic jet. J Fluid Mech 656:507–529

Schlegel M, Noack BR, Jordan P, Dillmann A, Groeschel E, Schroder W, Wei M, Freund JB, Lehmann O, Tadmor G (2012) On least-order flow representations for aerodynamics and aeroacoustics. J Fluid Mech 697:367–398

Sinha A (2011) Development of reduced-order models and strategies for feedback control of high-speed axisymmetric jets. PhD thesis, The Ohio State University

Sinha A, Kim K, Kim JH, Serrani A, Samimy M (2010a) Extremizing feedback control of a high-speed and high Reynolds number jet. AIAA J 48(2):387–399

Sinha A, Serrani A, Samimy M (2010b) Initial development of reduced-order models for feedback control of axisymmetric jets. Int J Flow Control 2(1):39–60

Tinney CE, Coiffet F, Delville J, Hall AM, Jordan P, Glauser MN (2006) On spectral linear stochastic estimation. Exp Fluids 41(5):763–775

Tinney CE, Glauser MN, Ukeiley LS (2008a) Low-dimensional characteristics of a transonic jet. Part 1. Proper orthogonal decomposition. J Fluid Mech 612:107–141

Tinney CE, Ukeiley LS, Glauser MN (2008b) Low-dimensional characteristics of a transonic jet. Part 2. Estimate and far-field prediction. J Fluid Mech 615:53–92

Ukeiley LS, Cordier L, Manceau R, Delville J, Glauser MN, Bonnet J-P (2001) Examination of large-scale structures in a turbulent plane mixing layer. Part 2. Dynamical systems model. J Fluid Mech 441:67–108

Utkin YG, Keshav S, Kim J-H, Kastner J, Adamovich IV, Samimy M (2007) Development and use of localized arc filament plasma actuators for high-speed flow control. J Phys D Appl Phys 40(3):685–694

Zheng X, Glauser MN (1990) A low dimensional description of the axisymmetric jet mixing layer. ASME Comput Eng 2:121–127